electronics

MDPI

Article

Design and Equivalent Circuit Model Extraction of a Fractal Slot-Loaded 3–40 GHz Super Wideband Antenna

Wasan Alamro [1,*], Boon-Chong Seet [1], Lulu Wang [2,3] and Prabakar Parthiban [4]

[1] Department of Electrical and Electronic Engineering, Auckland University of Technology, Auckland 1010, New Zealand; boon-chong.seet@aut.ac.nz
[2] Department of Engineering, Reykjavík University, 101 Reykjavík, Iceland; luluw@ru.is
[3] Department of Physiology and Biomedical Engineering, Mayo Clinic, Rochester, MN 55905, USA
[4] Engineering-Leadership Department, Sofant Technologies, Edinburgh EH3 8AN, UK; prabakarparthiban@gmail.com
* Correspondence: wasan.alamro@autuni.ac.nz

Abstract: In this paper, we present the design and equivalent circuit model (ECM) of a fractal slot-loaded super wideband (SWB) antenna for compact and high-performance applications operating in the 3–40 GHz range. The proposed antenna features a compact dimension of 40 × 35 × 1.57 mm³, a measured bandwidth ratio of 13:1, a peak gain of 9.7 dBi, an average radiation efficiency of 94%, and a low cross-polarization level across the entire bandwidth. The presented ECM is derived using transmission line theory and incorporates the individual behavior of each constituting element of the antenna. A dual sequential optimization approach is employed to determine the optimal element values. The ECM results show good agreement with both simulated and measured results in terms of the magnitude of reflection coefficient $|S_{11}|$ and both real and imaginary impedances with low mean absolute percentage errors of 4.9%, 7.5%, and 7.7%, respectively, demonstrating the model's ability to accurately predict the antenna's performance.

Keywords: equivalent circuit modeling; optimization; fractal slot; super wideband antenna; lumped elements; transmission line theory

Citation: Alamro, W.; Seet, B.-C.; Wang, L.; Parthiban, P. Design and Equivalent Circuit Model Extraction of a Fractal Slot-Loaded 3–40 GHz Super Wideband Antenna. *Electronics* **2024**, *13*, 4380. https://doi.org/10.3390/electronics13224380

Received: 15 October 2024
Revised: 5 November 2024
Accepted: 6 November 2024
Published: 8 November 2024

1. Introduction

The frequency range spanning from 3 GHz to 40 GHz is used by numerous current and emerging applications, including wireless communications (e.g., 5G C-band/mmWave, WiFi 5/6/6E/7), satellite broadcasting (e.g., Ku/Ka-bands), radar systems (e.g., L/S/X-bands for air traffic control, C-band for weather tracking), remote sensing (e.g., X-band for earth observation), and microwave medical imaging (e.g., S-band for deep tissue, K/Ka-bands for superficial tissue), among others [1]. Super wideband (SWB) antennas are defined as antennas that possess a bandwidth ratio of at least 10:1 [2]. For one that operates in the frequency range of 3–40 GHz proposed in this paper, the bandwidth ratio is over 13:1, which qualifies it to be classified as an SWB antenna. This broad bandwidth allows it to meet the diverse frequency requirements of many antenna applications; or to enhance a specific antenna application such as imaging, whose performance increases with the bandwidth of the antenna [3–5]. Key design parameters, including operating bandwidth, gain, radiation efficiency, design complexity, and fabrication cost, are well-aligned with the advantages of SWB technology [2,4–6].

Modeling the equivalent circuit of an antenna can offer an effective means of gaining insights into its behavior and thus a deeper understanding of its performance [7]. Therefore, in addition to designing a compact high-performance SWB antenna, this paper further explores the use of equivalent circuit models (ECMs) for analyzing the behavior of the designed SWB antenna.

Recent studies have explored various antenna configurations that leverage the benefits of SWB technology [8,9] and have identified key features, such as remarkable bandwidth and high polarization purity, that are crucial for enhancing performance in 5G networks and modern communication systems [10,11]. For instance, a coplanar waveguide (CPW)-fed SWB antenna, which features a modified bow-tie-shaped vertical patch with two asymmetrical ground planes is presented in [2]. Similarly, CPW feeding is used to enhance the impedance bandwidth of the SWB antenna in [12,13]. Another technique integrates fractal slots into the antenna structure for extending the lower frequency limit of its operating bandwidth [14,15]. Additionally, FSS is used in [16] to enhance surface current distribution, resulting in antenna gain enhancement. Moreover, a trapezoidal-shaped ground plane is investigated in [4] for a pentagonal UWB fractal antenna in order to improve impedance matching. This antenna operates in the range of 3–12.7 GHz with a fractional bandwidth (FBW) of 123.56%. However, the ECM is not discussed in this study. Similarly, [5] presents a Z-shaped UWB antenna for both microwave imaging and wireless communications, incorporating a stepped meander line structure to enhance bandwidth and radiation efficiency. The ECM is again not covered. Other studies in [17,18] presented SWB antennas along with their ECMs. In [17], a rectangular SWB antenna exhibiting 7.8 dBi gain and 94.5% radiation efficiency is proposed. In [18], a hexagonal SWB antenna with a peak gain of 7.28 dBi is presented. For both SWB antennas, their ECMs are based on a quasi-Newton optimization method and are not found to be accurate at high frequencies due to the complexity of high-order modes. Another SWB antenna with a peak gain of 5 dBi and an ECM is proposed in [19]. The ECM is based on the antenna's geometry and is found to offer limited accuracy at certain frequency ranges of its operating bandwidth. The authors in [20,21] have presented lumped-element-based ECMs for fractal SWB antennas. However, these ECMs are either too complex or lack sufficient accuracy. Similarly, empirically based ECMs for on-chip SWB antennas in [22,23] showed deviations in their results from expected form in a frequency range that spans over 45% of the operating bandwidth.

Further optimization of ECMs has been investigated [24–28]. For instance, [24] uses multi-objective particle swarm optimization to obtain the optimal ECM values of a frequency-selective surface (FSS), providing approximate predictions for the frequency range of 2.62–2.83 GHz. Another study [25] proposes an ECM for a UWB multi-input multi-output (MIMO) antenna with dimensions of $33 \times 17.8 \times 1.53$ mm^3, operating between 3 and 11.8 GHz with a 3.25 dBi peak gain and 93% radiation efficiency. However, the presented ECM fails to align with the antenna response in the 7.5–11.8 GHz range, and lacks discussion on mathematical relationships with transmission line theory. The authors of [26] present an ECM for a triple-band substrate integrated waveguide (SIW) cavity-backed slot antenna, resonating at 7.39, 9.43, and 14.79 GHz with gains of 3.2, 4.9, and 4.7 dBi, respectively. Despite good agreement with simulations, the ECM has a very narrow bandwidth of 250 MHz (2.67%).

In [27], an ECM is described for a circular UWB antenna with U-shaped parasitic strips, operating in the range of 2.85–12 GHz with a 4.7 dBi peak gain. Although the ECM is optimized using Keysight's Advanced Design System (ADS), the accuracy is inadequate, particularly between 8 and 12 GHz. Additionally, in [28], an ECM for a 60×60 mm^2 MIMO UWB antenna is presented. It is also optimized using ADS, but with poor accuracy in the 2–4 GHz range.

The analysis of these works shows that there remains room for further improvement of SWB antenna performance, particularly in terms of peak gain and bandwidth ratio. In addition, the existing works consistently show that challenges remain to realizing accurate ECMs for SWB antennas at high frequencies. In this paper, we attempt to address these gaps by presenting a new SWB antenna design with superior performance and a dual sequential optimization approach to enhance ECM accuracy. Our objectives are twofold. First, we aim to design and validate the real-world performance of an enhanced SWB antenna through experimental analysis in both frequency and time domains. Additionally, we seek to explore an effective and efficient approach to optimizing the ECM of our SWB antenna.

Our main contributions are summarized as follow:

- We designed a new fractal-loaded patch antenna that features a measured super-wide bandwidth spanning 3.1–40 GHz, a high peak gain of 9.7 dBi, a high average radiation efficiency of 94%, and high polarization purity across the entire bandwidth.
- We developed an ECM of our designed antenna that models accurately even at high frequencies, based on a dual sequential optimization approach, known antenna geometry, and transmission line theory.
- We investigated, for the first time in the literature, a dual sequential optimization approach combining gradient and quasi-Newton methods, which demonstrates fast convergence and high modeling accuracy.

The rest of the paper is organized as follows. Section 2 presents the design of our SWB antenna and its evolution process in detail. Section 3 further presents the ECM of our SWB antenna. Section 4 describes the antenna fabrication and measurement setup. Section 5 discusses and compares the simulated and measured results of the fabricated antenna. Finally, Section 6 concludes the paper.

2. Design of SWB Antenna and Its Evolution Process

2.1. Antenna Geometry and Evolution

This section describes the structure and evolution of our SWB antenna, which utilizes the Rogers RT/Duroid 5870 substrate (ε_r = 2.33, $tan\delta$ = 0.0012) and has physical dimensions of 40 × 35 × 1.57 mm^3, as shown in Figure 1. Extensive parametric studies have been performed using the Ansys High Frequency Structure Simulator (HFSS), and the final optimized design parameters are summarized in Table 1. The evolution of our SWB antenna design is illustrated in Figure 2, progressing from the initial design "antenna 0" to the final design "antenna 8". Their corresponding simulated magnitude of reflection coefficient $|S_{11}|$ (dB) results are shown in Figure 3.

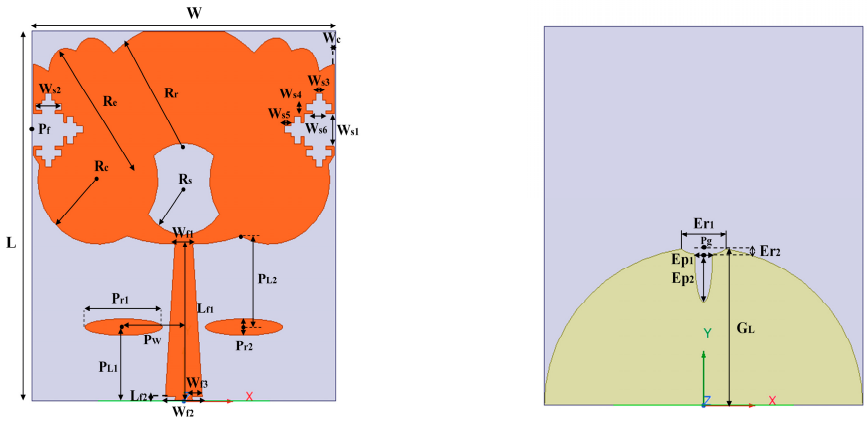

(**a**) (**b**)

Figure 1. SWB antenna structure: (**a**) front view; (**b**) bottom view.

The initial design in Figure 2a featured a simple circular patch paired with a semi-elliptical ground plane. This design exhibited a relatively narrow bandwidth. Various modifications were then progressively made to enhance the antenna performance, as illustrated from Figure 2b–i.

Figure 2b shows the introduction of a tapered feedline to improve impedance matching between the 50 Ω coaxial cable connected to the 2.92 mm K-type connector and the high impedance at the patch's edge. Next, intersecting ellipses were incorporated into the circular patch, as shown in Figure 2c. This modification increased the antenna's electrical length, resulting in a broader bandwidth and improving $|S_{11}|$ to −14.7 dB at the first resonant frequency.

Table 1. Optimized values of the proposed antenna.

Param.	Value (mm)	Param.	Value (mm)	Param.	Value (mm)
W	35	Wf1	2	Re	4
L	40	Wf2	4.3	Wc	0.15
Ws1	3.5	Wf3	1.16	Pr1	9
Ws2	3	Pr2	1.8	Pw	7
Ws3	0.75	Lf1	17	PL1	8
Ws4	1.5	Lf2	0.5	PL2	9.87
Ws5	0.75	Rr	12	Er1	2.5
Ws6	1.5	Rs	5	Er2	0.75
Pf	29.4	Rc	7	Ep1	2
GL	16.7	Pg	16.7	Ep2	5

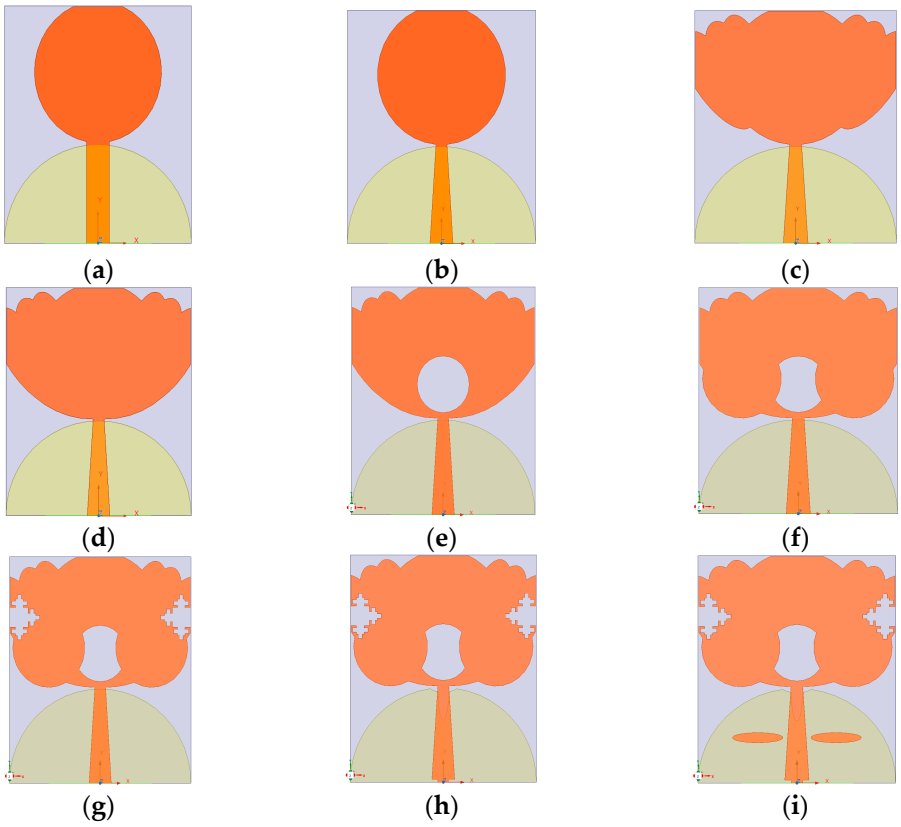

Figure 2. SWB antenna design evolution: (**a**) antenna 0; (**b**) antenna 1; (**c**) antenna 2; (**d**) antenna 3; (**e**) antenna 4; (**f**) antenna 5; (**g**) antenna 6; (**h**) antenna 7; and (**i**) final antenna 8.

Figure 2d depicts the addition of a polygon to smooth the transition of surface current at the edge of the patch. This improved the $|S_{11}|$ levels at the first two resonant frequencies, achieving −16.3 dB and −42.6 dB at 4.1 and 9.3 GHz, respectively. Incorporating slots of various shapes, lengths, and positions into the main radiator notably impacted the antenna performance, particularly in terms of shifting the resonance frequencies. For instance, a circular slot added to the center of the patch, as shown in Figure 2e, shifted the second resonant frequency to 8.3 GHz and enhanced impedance matching in the 18.7–19.2 GHz range. The optimal position and radius of this slot were determined through parametric simulations. Further modifications included adding two circles to the circular radiator, as depicted in Figure 2f. This adjustment increased the electrical length and enhanced the patch's inductive nature, improving impedance matching, extending the bandwidth from 2.5 GHz to 37 GHz, and shifting the first resonant frequency to 3.8 GHz, with an improved $|S_{11}|$ of −26.7 dB. Subsequently, two fractal slots with duplicated rectangular shapes were introduced on both sides of the radiator, as shown in Figure 2g. These slots

further extended the electrical length and enhanced the first resonant frequency, achieving a $|S_{11}|$ of −32.2 dB at 3.9 GHz. Despite the improvements, two notches in performance were observed around 18 GHz and in the 30–31 GHz range. To address these issues, two elliptical slots were introduced into the ground plane, and a rectangular slot was added at the edge of the feedline, as shown in Figure 2h. These adjustments helped fine-tune the capacitive coupling between the patch plane and the ground plane, resulting in enhanced impedance matching. Consequently, the bandwidth was extended to cover the frequency range of 2.5–35.3 GHz, with improved $|S_{11}|$ values of −36 dB and −40.3 dB at the first and second resonant frequencies of 3.8 and 7.7 GHz, respectively.

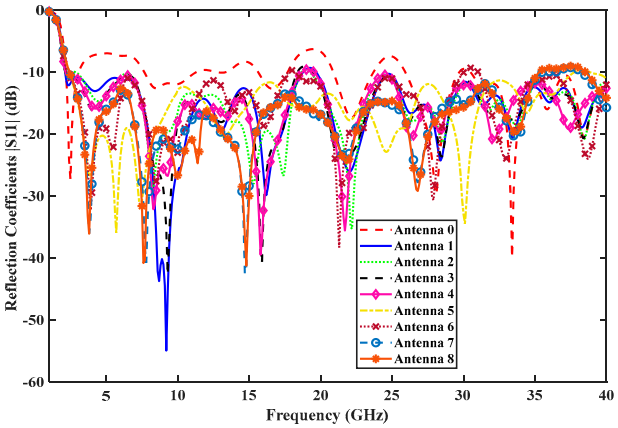

Figure 3. Simulated $|S_{11}|$ results of different antenna stages.

Finally, two elliptically shaped parasitic elements were added to each side of the tapered feedline, as shown in Figure 2i. These elements were not electrically connected to the patch; instead, they resonated in response to the radiator's influence. With the incorporation of these parasitic elements, impedance matching was notably improved, particularly within the frequency range of 9.3–12 GHz. As a result, the overall bandwidth expanded to cover the frequency range of 2.5–35.4 GHz, achieving a bandwidth ratio of 14.2:1 as illustrated in Figure 3.

2.2. Parametric Studies

In this section, different parameters of the proposed antenna were optimized by varying one parameter at a time while keeping other parameters to their initial default values. This approach helped to study the effect of different dimension parameters on the antenna performance over its bandwidth using a quasi-Newton optimizer in HFSS. Starting with the initial antenna (antenna 0), different parameters were optimized to achieve optimal performance.

The radius of the circular patch was increased from 10 mm to 13 mm in steps of 1 mm. As shown in Figure 4a, the optimal radius was found to be 12 mm, which offers the best impedance matching. Likewise, the width of the bottom feedline was increased from 2.3 mm to 5.3 mm in steps of 1 mm, and the optimal width was found to be 4.3 mm. This resulted in the best $|S_{11}|$ of −27 dB at the first resonant frequency, as shown in Figure 4b.

Following the introduction of a circular slot in the center of the patch element (antenna 4), the impact of different slot radii, which were increased from 4.5 mm to 5.5 mm in steps of 0.5 mm was investigated. The results in Figure 4c indicate that a slot radius of 5 mm provides the most favorable impedance matching, particularly at higher frequency bands.

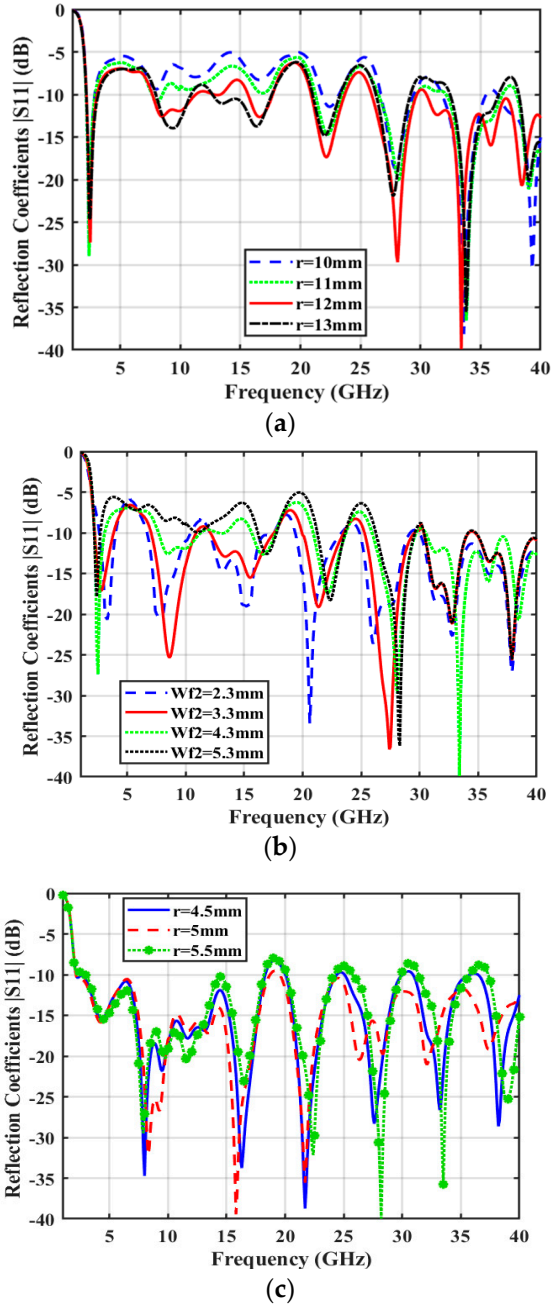

Figure 4. Simulated $|S_{11}|$ results under varying (**a**) patch radius; (**b**) bottom feedline width; and (**c**) patch slot radius.

3. ECM Extraction of SWB Antenna

This section details the ECM of our SWB antenna, including its parameter extraction, and validation of the circuit model.

3.1. Circuit Modeling of Antenna Elements

The geometry of the antenna and corresponding circuit model for each component are shown in Figure 5. The ECM was developed by analyzing the antenna structure and electromagnetic (EM) properties. It comprises several components, each having a certain influence on the antenna performance. The primary component is the radiating patch, which is crucial for emitting EM waves. It acts as a bandpass filter and is modeled as a parallel RLC branch with a series inductor, representing the inductive nature of the radiating patch at high frequencies [29–32]. The parallel resistor and inductor account for

the losses and inductive properties in the patch, respectively, while the parallel capacitor represents the capacitance between the patch and ground plane.

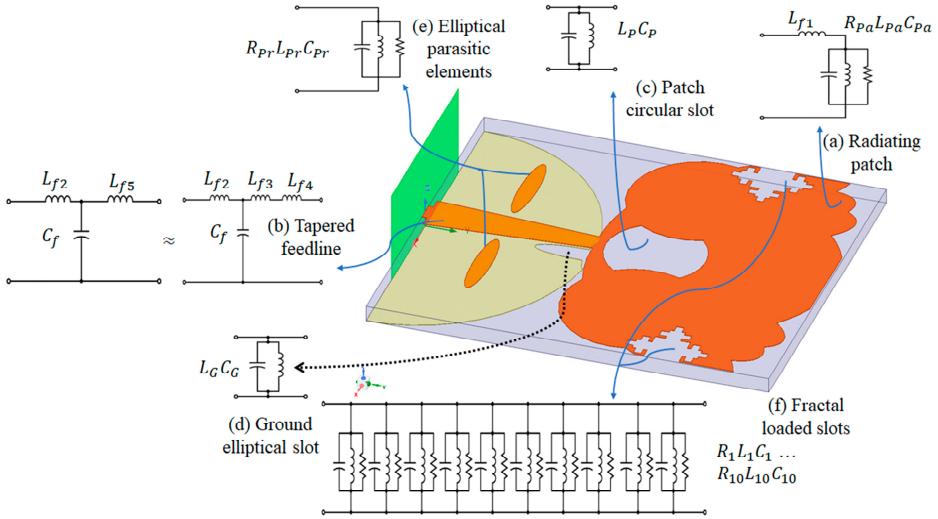

Figure 5. SWB antenna geometry and circuit model of each element.

The feed configuration includes a rectangular and tapered feedline, which contributes to the patch's inductive nature [33]. The tapered feedline alters the impedance matching between the top and bottom of the microstrip line. This change is depicted by three series inductors and a parallel capacitor in the circuit model. The antenna's resonance is affected by the notches incorporated into the patch and ground plane. A parallel LC circuit models the slots in the middle of the circular patch and elliptical slots in the ground [34]. The two elliptically shaped parasitic elements introduced on each side of the tapered feedline are represented as a parallel RLC branch. These elements are not electrically connected to the patch. Instead, they resonate in response to the radiator's influence.

Fractal slots, which consist of duplicated rectangular slots of varying dimensions, are added to both sides of the circular patch. These fractal slots enhance the antenna's bandwidth but complicate the ECM. Each fractal slot is modeled as a parallel resonant circuit [27], acting as a bandpass filter to allow specific frequencies to pass while attenuating others. Given that each fractal slot comprises 10 rectangles, it is modeled as 10 parallel RLC branches. Hence, 20 parallel RLC circuits are incorporated for two fractal slots on each side of the patch.

3.2. Full Lumped Element ECM

To simplify the physical ECM into a lumped-element model, we combined the 20 parallel RLC circuits into 10 equivalent parallel RLC branches ($R_1L_1C_1 \ldots R_{10}L_{10}C_{10}$). This reduction was feasible because the fractal slots are identical and share the same dimensions. Next, we assembled two parallel branches, $R_{Pa}L_{Pa}C_{Pa}$ and $R_{Pr}L_{Pr}C_{Pr}$, into a single parallel $R_{11}L_{14}C_{13}$ branch. Additionally, the parallel LC branches, L_PC_P and L_GC_G, were merged into a parallel $L_{11}C_{11}$ branch. The feedline inductors L_{f3} and L_{f4} were combined into L_{f5}, which was subsequently merged with L_{f1} into L_{13}. The complete circuit configuration is depicted in Figure 6, where C_f corresponds to C_{12}, and L_{f2} corresponds to L_{12}. Figure 6 illustrates the full lumped-element ECM of our SWB antenna. Several optimization goals were defined based on the main resonant frequencies and their corresponding $|S_{11}|$ extracted from simulated results, as listed in Table 2.

Gradient and quasi-Newton methods were employed to determine the ECM's optimal lumped-element values that best matched the realistic simulated data obtained using Keysight's Advanced Design System (ADS). These methods differ in their approach to updating lumped-element values during optimization. The gradient method computes a cost function to evaluate the importance of the lumped elements and updates their values

in the direction of the gradient (steepest descent). This method tends to converge quickly to a local minimum but can be sensitive to the initial values and frequency step size used for updating the importance.

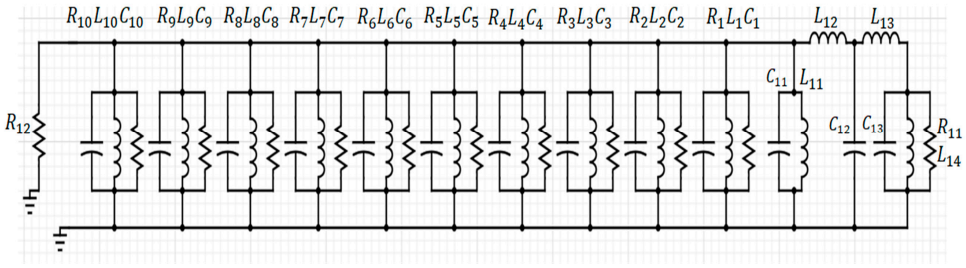

Figure 6. Full lumped-element ECM of SWB antenna.

Table 2. Defined goals for optimizers.

Goal #	$\lvert S_{11} \rvert$ (dB)	Frequency (GHz)
1	−36	3.8
2	−40.8	7.6
3	−28.5	10
4	−34.9	14.8
5	−24.8	21.8
6	−29.2	26.8
7	−20	33.8

In this paper, we set the initial RLC values to R = 0.001 Ω, L = 0.001 nH, and C = 0.001 pF, frequency step size to 0.1 GHz, and number of iterations to 1000. A limit line was defined for each goal, specifying the acceptable response based on the $\lvert S_{11} \rvert$ extracted from the simulator, the relationship between the limit line (min/max) and the response, and the weight factor (WF) for the limit line. All WF values were set to 1. The actual WF used in the error function calculation was the product of the goal WF and the limit line WF. If greater emphasis is needed on a particular goal, its WF can be increased.

On the other hand, the quasi-Newton method approximates the Hessian matrix to compute the direction of steepest descent, which allows for more efficient updates of the lumped element values, leading to a faster convergence, by considering the curvature of the cost function. It was employed as the second optimizer in our dual sequential optimization approach to further refine the ECM for improved matching performance. The least square error function was used as the error calculation function (ECF) given in (1) to achieve the desired performance:

$$ECF = \sum_{all\ goals} W_i \times |s_i - g_i|^2. \quad (1)$$

where W_i is the weighing factor for the ith goal, s_i is the ith frequency-dependent response being optimized, and g_i is the ith goal value over the defined frequency range. ECF is calculated by evaluating the error for each goal at each frequency point, and then squaring the magnitude of the error. Table 3 presents the optimized values of all lumped elements in our ECM.

Figure 7 compares the obtained $\lvert S_{11} \rvert$ performance, showing a good agreement between the modeled and simulated results. It also illustrates that the ECM can accurately reflect the simulated bandwidth, spanning from 2.5 to 40 GHz. Figure 8 presents the corresponding average root-mean-square errors (RMSE) and mean absolute percentage errors (MAPE). The low RMSE of 0.041 and MAPE of 4.9% confirm the accuracy of the presented model and the effectiveness of the optimization method used.

Table 3. Optimal lumped element values for ECM.

Param.	Value (Ω)	Param.	Value (nH)	Param.	Value (pF)
R_1	142.428	L_2	6.54311	C_1	0.0028622
R_2	37.3572	L_3	16.3512	C_2	0.49568
R_3	214.458	L_4	1498.73	C_3	0.003439
R_4	2.09613	L_5	2.54945	C_4	0.0074975
R_5	47.9401	L_6	7.40719	C_5	0.420298
R_6	66.8471	L_7	5.95808	C_6	0.0130909
R_7	75.2988	L_8	0.23312	C_7	0.0599383
R_8	70.2402	L_9	2.35217	C_8	0.116726
R_9	57.4437	L_{10}	12.354	C_9	0.0724266

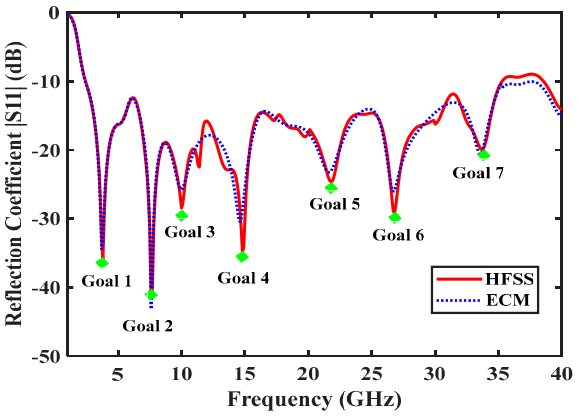

Figure 7. Comparison between modeled and simulated $|S_{11}|$.

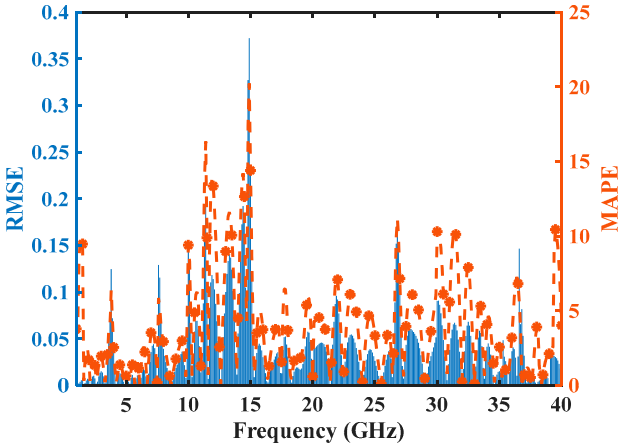

Figure 8. RMSE and MAPE between modeled and simulated $|S_{11}|$.

3.3. Analysis of ECM Using Transmission Line Theory

In this section, we apply the transmission line theory to analyze the ECM and simplify its structure as shown in Figure 9. This reduces the complexity of the antenna behavior to a few key parameters R, L, G, and C, which helps in reducing the computational requirements.

Additionally, the simplified model makes it easier to predict antenna performance and make design modifications. The process involves combining the 10 parallel RLC branches ($R_1L_1C_1 \ldots R_{10}L_{10}C_{10}$) representing the fractal slot effect into a single $R_{eq}L_{eq}C_{eq}$ branch. The distributed transmission line parameters R, L, G, and C are used to determine the equivalent circuit elements as follows:

$$R_{eq} = 1/\sum_{i=1}^{10} 1/R_i = 1.645107\ \Omega$$

$$L_{eq} = 1/\sum_{i=1}^{10} 1/L_i = 0.1729425\ nH$$
$$C_{eq} = \sum_{i=1}^{10} C_i = 1.2499628\ pF$$
$$G_{eq} = 1/R_{eq} = 0.6078632\ S$$

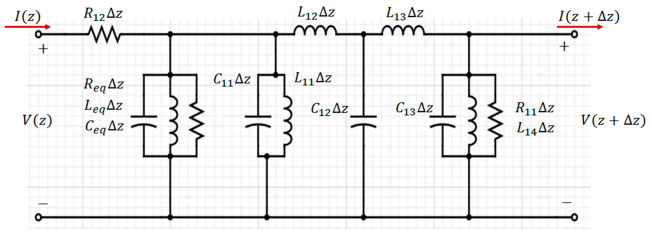

Figure 9. Simplified ECM using transmission line theory.

Applying Kirchhoff's voltage law to the circuit in Figure 9, where z and Δz represents the length and the differential length element of the transmission line, respectively:

$$V(z) - I(z)R_{12}\Delta z - I(z+\Delta z)j\omega L_{12}\Delta z - I(z+\Delta z)j\omega L_{13}\Delta z - V(z+\Delta z) = 0 \quad (2)$$

Rearranging (2) to separate the voltage and current terms and then dividing by Δz:

$$(V(z+\Delta z) - V(z))/\Delta z = -(I(z)R_{12}\Delta z)/\Delta z - (I(z+\Delta z)j\omega(L_{12}+L_{13})\Delta z)/\Delta z$$

Taking the limit as $\Delta z \to 0$:

$$(\partial V(z))/\partial z = -I(z)(R_{12} + j\omega(L_{12}+L_{13})) \quad (3)$$

Next, applying Kirchhoff's current law to the same circuit:

$$\begin{aligned} I(z) - V(z+\Delta z)\big(G_{eq}+G_{11}\big)\Delta z - V(z+\Delta z)j\omega\big(C_{eq}+C_{11}+C_{12}+C_{13}\big)\Delta z \\ -V(z+\Delta z)/j\omega\big(L_{eq}+L_{11}+L_{14}\big)\Delta z - I(z+\Delta z) = 0 \end{aligned} \quad (4)$$

Similarly, rearranging (4) to separate the voltage and current terms and then dividing by Δz:

$$\begin{aligned} &(I(z+\Delta z) - I(z))/\Delta z \\ &\quad = -V(z+\Delta z)\big[\big(G_{eq}+G_{11}\big) + j\omega\big(C_{eq}+C_{11}+C_{12}+C_{13}\big) \\ &\quad +1/j\omega\big(L_{eq}+L_{11}+L_{14}\big)\big]\Delta z/\Delta z \end{aligned}$$

Taking the limit as $\Delta z \to 0$:

$$(\partial I(z))/\partial z = -V(z)\big[\big(G_{eq}+G_{11}\big) + j\omega\big(C_{eq}+C_{11}+C_{12}+C_{13}\big) + 1/j\omega\big(L_{eq}+L_{11}+L_{14}\big)\big]$$

As $\omega\big(L_{eq}+L_{11}+L_{14}\big) \gg 1$, the term $1/j\omega\big(L_{eq}+L_{11}+L_{14}\big)$ could be neglected, giving:

$$(\partial I(z))/\partial z = -V(z)\big[\big(G_{eq}+G_{11}\big) + j\omega\big(C_{eq}+C_{11}+C_{12}+C_{13}\big)\big] \quad (5)$$

In frequency domain, the general solutions of (3) and (5) are exponential functions. Thus, they can be rewritten as:

$$V(z) = V_o^+ e^{-\gamma z} + V_o^- e^{\gamma z} \quad (6)$$

$$I(z) = I_o^+ e^{-\gamma z} + I_o^- e^{\gamma z} \quad (7)$$

where γ is the propagation constant, and their ratio gives the characteristic impedance (Z_o). Rearranging (3) to obtain an expression for the current and evaluating the partial derivative:

$$\begin{aligned} I(z) &= -1/((R_{12} + j\omega(L_{12} + L_{13})))(\partial V(z))/\partial z \\ &= -1/((R_{12} + j\omega(L_{12} + L_{13})))(V_o^+(-\gamma)e^{-\gamma z} + V_o^-(\gamma)e^{\gamma z}) \\ &= \gamma/((R_{12} + j\omega(L_{12} + L_{13})))(V_o^+ + e^{-\gamma z} - V_o^- e^{\gamma z}) \end{aligned} \tag{8}$$

where $\gamma = \sqrt{([R_{12} + j\omega(L_{12} + L_{13})][(G_{eq} + G_{11}) + j\omega(C_{eq} + C_{11} + C_{12} + C_{13})])}$.

Then Z_o can be found:

$$Z_o = V(z)/I(z) = \sqrt{((R_{12} + j\omega(L_{12} + L_{13}))/((G_{eq} + G_{11}) + j\omega(C_{eq} + C_{11} + C_{12} + C_{13})))} \tag{9}$$

To find the impedance at the first resonant frequency (3.8 GHz) of our SWB antenna, substituting this frequency into (9) yields $Z_o = 50.81 + j1.53\ \Omega$, which closely matches the simulated Z_o in Figure 10. The overall low RMSEs of 0.243 and 0.254 (with corresponding low MAPEs of 7.5% and 7.7%) depicted in Figure 11 for the real and imaginary complex impedance Z_o, respectively, confirm that the simplified ECM can still accurately model the characteristics of our SWB antenna.

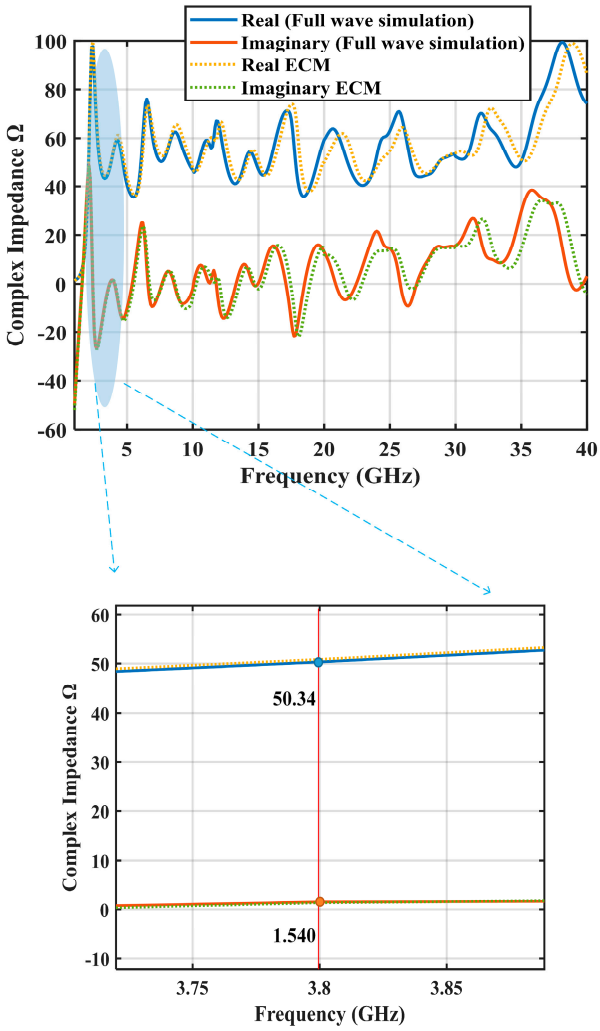

Figure 10. Simulated complex impedance Z_o of our SWB antenna.

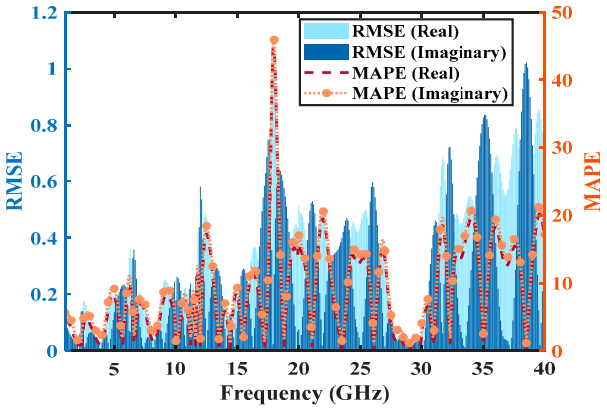

Figure 11. RMSE and MAPE between modeled and simulated complex impedance Z_o of our SWB antenna.

4. SWB Antenna Fabrication and Measurement Setup

The proposed SWB antenna was fabricated on Rogers RT/Duroid 5870 substrate of thickness 0.062" (1.575 mm) and 1 oz. (0.35 µm) H1/H1 copper cladding. An immersion silver finish was applied to the surface to protect it against any oxidation and improve the signal quality at high frequency. Figure 12 shows the fabricated SWB antenna. In addition to simulations using HFSS and ADS, measurements were performed using an Anritsu S820E vector network analyzer (VNA) in a radio frequency (RF) anechoic chamber (Figure 13). All radiation pattern measurements were conducted under far-field conditions with the aid of an antenna positioner controlled by a custom MATLAB program. Horn antennas covering the frequency range of 3–40 GHz were utilized for these measurements. The results were acquired using VNA advanced mode, and the external cables that operate from DC to 40 GHz were calibrated once connected to the VNA ports to calibrate out any frequency response originates from the cables and to obtain high quality measurements. The calibration algorithm used in this research was two ports SOLT (short-open-load-thru).

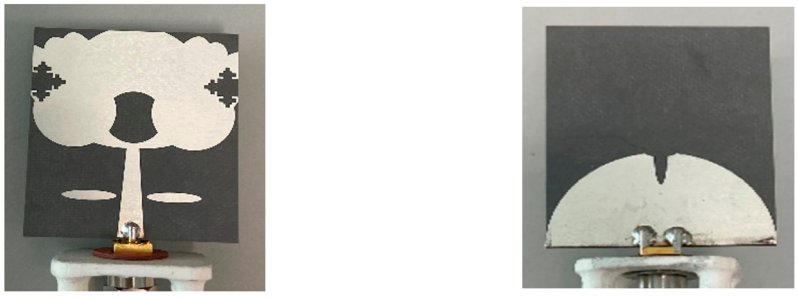

(**a**) (**b**)

Figure 12. Fabricated SWB antenna: (**a**) top view; (**b**) bottom view.

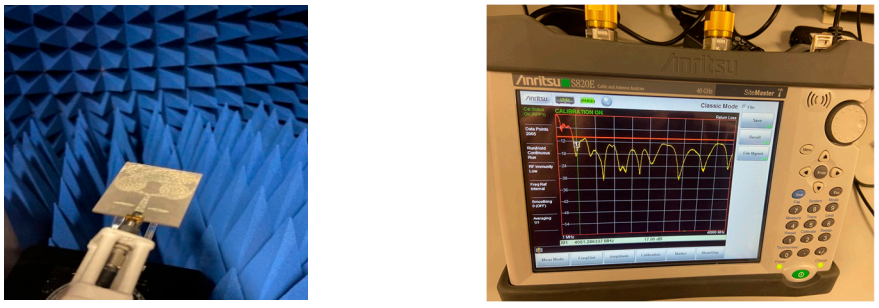

(**a**) (**b**)

Figure 13. (**a**) SWB antenna measurement in RF anechoic chamber; (**b**) $|S_{11}|$ measurement using VNA.

5. Results and Discussion

This section discusses the simulated and measured results of the proposed SWB antenna. Figure 14 shows relatively good agreement between simulated and measured $|S_{11}|$ values. However, slight variations are observed, likely due to fabrication tolerances. The results also show similar simulated and measured fractional bandwidth of 173.6% (2.5–35.4 GHz) and 171.23% (3.1–40 GHz), respectively, corresponding to a respective bandwidth ratio of approximately 14:1 and 13:1. The next three sub-sections further analyze the antenna's surface current distribution and radiation pattern, as well as the effects of mutual coupling when it operates in pairs under face-to-face or side-by-side configurations in close proximity.

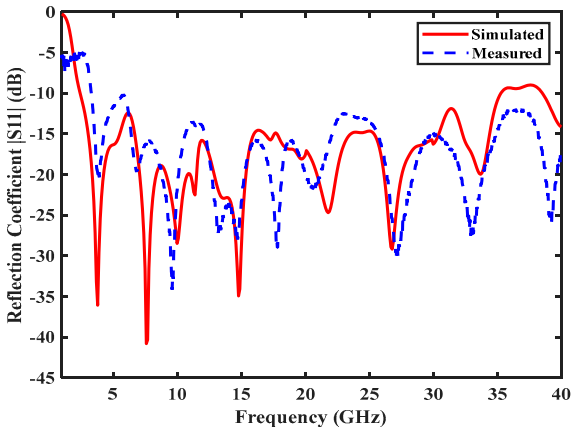

Figure 14. Comparison between simulated and measured $|S_{11}|$.

5.1. Surface Current Distribution and Radiation Pattern

The simulated surface current distributions at each of the first six resonant frequencies listed in Table 2 are shown in Figure 15. Notable current concentration in the feedline provides insights into the mode variation. In Figure 15a, the first-order harmonic resonance (fundamental mode) at 3.8 GHz is clearly observed, with radiated power predominantly confined to the front side of the antenna. This is due to the current concentrating along the lower side of the fractal slot-loaded radiator. In Figure 15b, the second-order harmonic becomes tangible, with the current distribution focused on the lower portion of the radiating patch. The current also propagated in the lower segments of the fractal slots, leading to a standing wave in the top section of the radiator and creating a radiating null.

At the higher resonance of 10 GHz as shown in Figure 15c, the current was more concentrated at the lower circular edges of the radiator. In this case, the far-field pattern exhibits a donut-shaped structure, with most of the radiated power concentrated around the antenna's front side and upper section of the radiator, which increases the size of the radiating null at the top of the antenna. As frequency increased, the higher-order modes became more apparent, as evidenced by the complex current distribution at 14.8, 21.8, and 26.8 GHz in Figure 15d–f. Consequently, the current predominantly traversed various distributed locations along the edges of the tapered radiator, resulting in significant null points on the radiator's surface.

The antenna's radiation pattern was evaluated in both E-plane (YZ-plane, $\varphi = 90°$) and H-plane (XZ-plane, $\varphi = 0°$) at various frequency points. Generally, the antenna maintained an almost omnidirectional configuration in both E- and H-planes at lower frequencies. However, as frequency increases, some distortions occurred due to excitation of higher-order modes. Figure 16 shows the radiation pattern at the first resonance (3.8 GHz) and last resonance (33.8 GHz). The measured and simulated results are close. Figure 17 further illustrates the co- and cross-polarization radiation patterns at the first and last resonance. The proposed SWB antenna exhibited low cross-polarization levels, achieving polarization purities of 40 dB and 20 dB at 3.8 and 33.8 GHz, respectively.

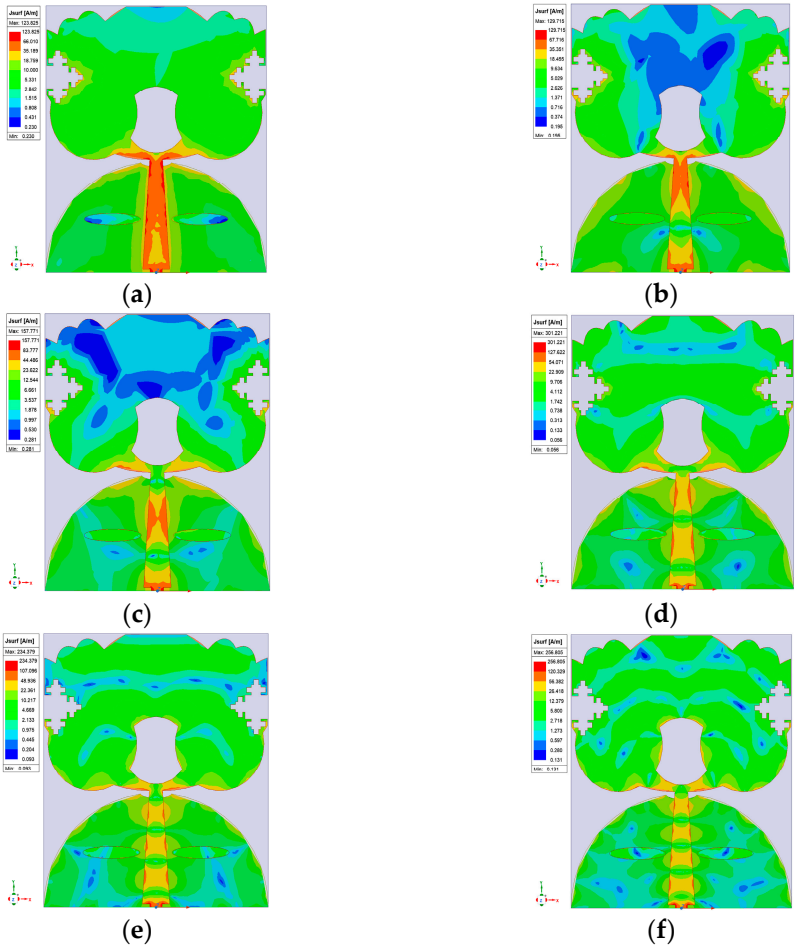

Figure 15. Surface current distribution at (**a**) 3.8 GHz, (**b**) 7.6 GHz, (**c**) 10 GHz, (**d**) 14.8 GHz, (**e**) 21.8 GHz, and (**f**) 26.8 GHz, corresponding to the first six resonant frequencies of our SWB antenna.

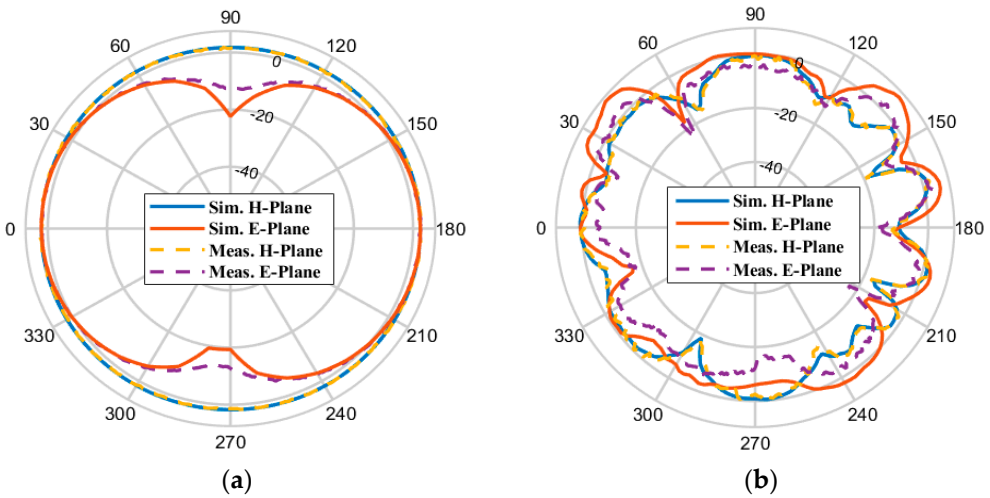

Figure 16. Simulated and measured 2D radiation pattern at (**a**) 3.8 GHz and (**b**) 33.8 GHz, corresponding to the first and last resonant frequencies of our SWB antenna.

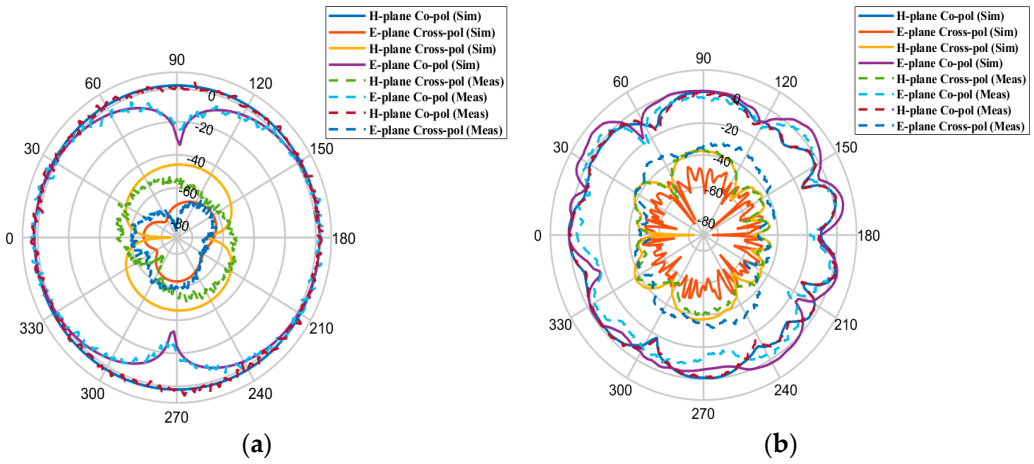

Figure 17. Simulated and measured co- and cross polarization radiation patterns at (**a**) 3.8 GHz and (**b**) 33.8 GHz, corresponding to the first and last resonant frequencies of our SWB antenna.

5.2. Realized Gain and Radiation Efficiency

Realized gain measurement was performed using two identical SWB antennas under far-field conditions. Figure 18 shows the simulated and measured broadside realized gain of the antenna. The results indicate that the gain generally increases with frequency and remains consistently positive across the entire bandwidth. This trend can be attributed to the effective aperture of the patch being larger than the wavelength at higher frequencies. Since antenna gain is directly related to the antenna effective aperture and signal wavelength, it generally improves with frequency. However, at higher frequencies, gain attenuation can occur due to connector losses. The antenna exhibited 3.4 dBi at the first resonant frequency of 3.8 GHz, and its peak gain of 9.7 dBi at 39.5 GHz, showing a strong agreement with the simulated results.

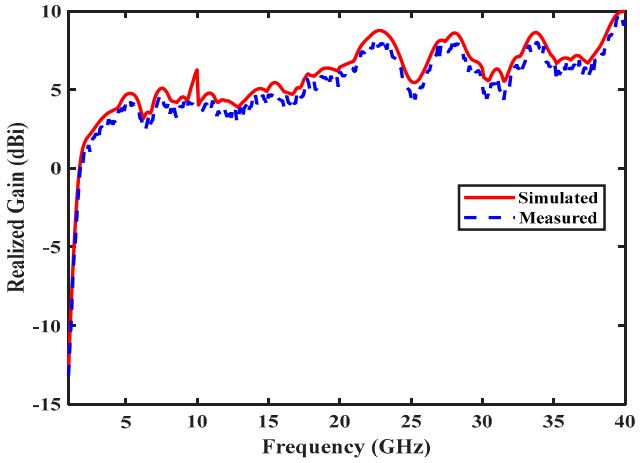

Figure 18. Simulated and measured realized gain.

Figure 19 illustrates the antenna's radiation efficiency, which generally maintained at high efficiency across the bandwidth. The average efficiency was 94%, with a peak measured efficiency of 97.9% attained at 9.7 GHz. However, beyond 22 GHz, there was a gradual decline in the radiation efficiency attributed to increased impedance mismatch caused by higher-order modes. Notably, high measured radiation efficiencies of 97.1% and 95.6% were achieved at the first and second resonant frequencies of 3.8 GHz and 7.6 GHz, respectively.

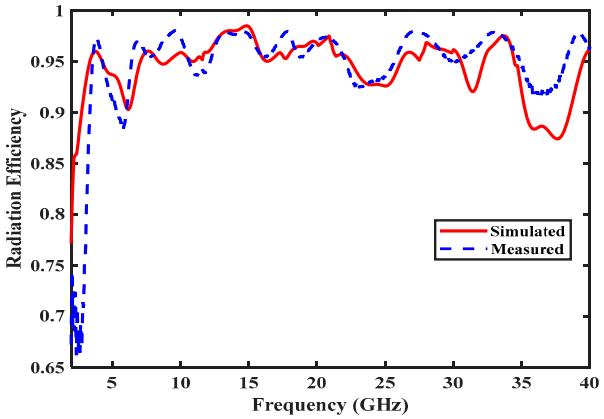

Figure 19. Simulated and measured radiation efficiency.

5.3. Group Delay, Isolation and Phase Variation

For effective deployment of antennas in any application, it is critical to evaluate the time domain signal characteristics of the antennas in different deployment configurations. Minimizing mutual coupling between adjacent antennas is necessary to reduce co-interference and maintain high signal integrity [34–36]. The two deployment structures impact 5G and 6G wireless communications by enhancing signal reliability, efficiency, and stability, which are essential for real-time applications that demand ultra-low latency and high data throughput [37]. In microwave imaging, the stable group delay provided by these structures improves image clarity and accuracy, facilitating early detection of anomalies like tumors and supporting advanced telemedicine applications [38].

Time domain analysis was performed to examine the antenna's dispersion characteristics. Two deployment configurations were considered: face-to-face and side-by-side, as shown in Figure 20a and Figure 20b, respectively, each consisting of two identical antennas separated by their minimum far-field distance (760 mm).

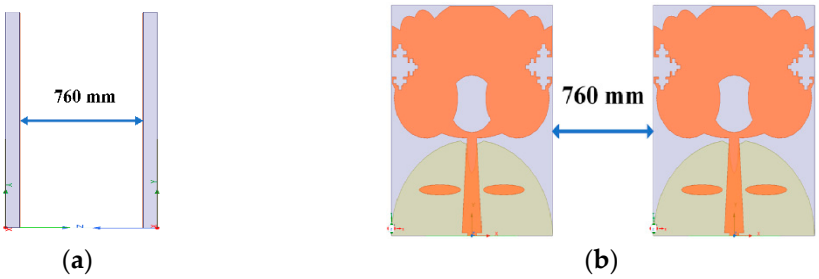

Figure 20. (**a**) Face-to-face and (**b**) side-by-side configuration.

A key time domain parameter is the group delay, which can be calculated as the negative derivative of phase variation:

$$\tau_g(\omega) = -\frac{d\varphi(\omega)}{d\omega} = -\frac{d\varphi(\omega)}{2\pi df} \tag{10}$$

To maintain an accurate linear phase response and coherent transmission over the operating frequency range, it is essential to achieve minimal group delay, typically less than 2 ns [39]. Figure 21 shows the measured group delay was under the limit for both configurations. Furthermore, Figure 22a demonstrates high isolation (<−30 dB) that ensures low mutual coupling between adjacent antennas. The phase variations depicted in Figure 22b are consistent, indicating that the received signals were free from significant phase distortion [40]. This consistency resulted in improved signal integrity and reduced distortion.

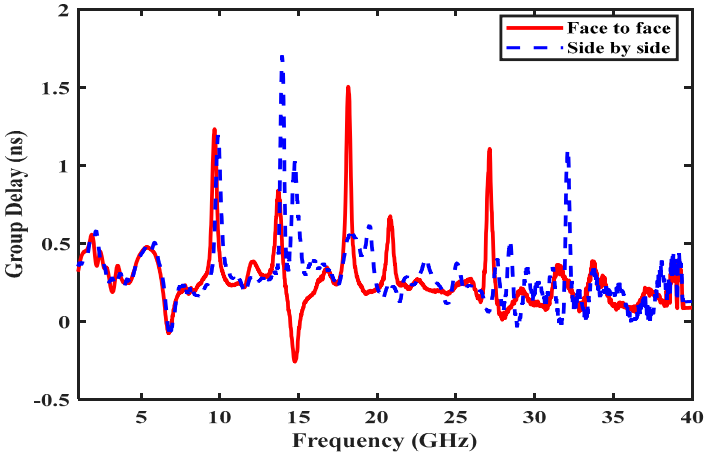

Figure 21. Measured group delay.

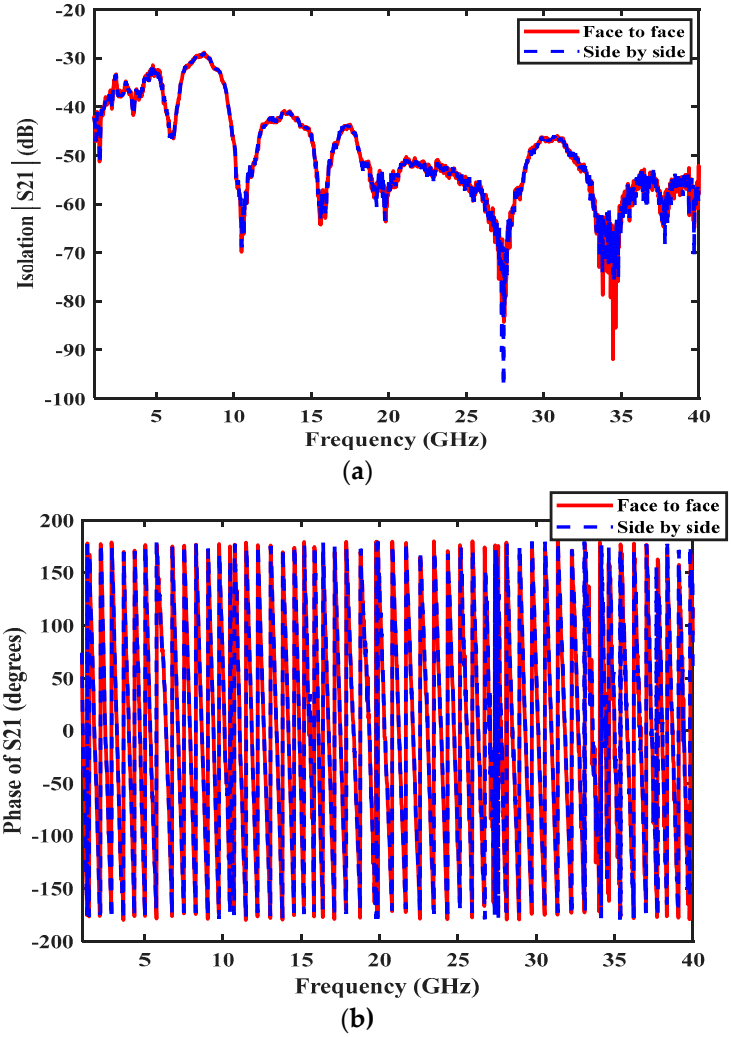

Figure 22. Measured (**a**) isolation and (**b**) phase variation.

Finally, a comparison between the proposed antenna and related works in the literature in terms of their features and performances is summarized in Table 4.

Table 4. Comparison between the proposed antenna and related works in the literature.

Ref. No.	Size (mm^3)	OFR (GHz)	% BW	Peak Gain (dBi)	Radiation Efficiency (Min, Max)%	$\lvert S_{11} \rvert$ Levels @ f_{r1}, f_{r2}, f_{r3} (dB)	ECM	ECM Accuracy Avg MAPE, Avg RMSE
[2]	24.5 × 20 × 1.6	3.035–17.39	140.56	4.56	40, 89.36	−13 dB @ 3.2 GHz −17.7 dB @ 4.39 GHz −28.4 dB @ 6 GHz	No	--
[4]	30 × 24 × 0.787	3–12.7	123.56	3.6	82, 96	−19.7 @ 4.5 GHz −27 dB @ 8.8 GHz	No	--
[5]	38 × 35 × 1.57	2.8–22.7	156	6.4	70, 93	−25 dB @ 3.6 GHz −29 dB @ 4.3 GHz	No	--
[17]	40 × 35 × 1.5	2.7–20.3	153.04	7.8	75, 94.5	−15.8 dB @ 3 GHz −15.7 @ 5 GHz −18.6 dB @ 7.8 GHz	Yes	Weak accuracy at high frequency band, MAPE (23.12%), RMSE (0.265)
[18]	36 × 36 × 1.6	3.37–27.71	156.6	7.28	70, 96	−19.5 dB @ 4.1 GHz −13.1 dB @ 6.7 GHz −13.1 dB @ 7.9 GHz	Yes	Weak accuracy at high frequency band, MAPE (19.55%), RSME (0.332)
[19]	25.2 × 23.4 × 1.413	2.45–20	156	5	65, 90	−20 dB @ 2.6 GHz −25.3 dB @ 3.9 GHz −15.8 dB @ 5 GHz	Yes	Accuracy not good at high and low frequency bands (4–5, 5.5–7, 13.5–19) GHz, MAPE (24.9%), RMSE (0.285)
[21]	36 × 32 × 1.6	2–13.8 14.67–20	149.36 30.75	5.4	70, 93	−20.8 dB @ 2.5 GHz −33.2 dB @ 2.8 GHz −21.8 dB @ 5 GHz	Yes	NA
[25]	33 × 17.8 × 1.53	3–11.8	118.92	3.25	93, 94	−21 dB @ 4.3 GHz −20.2 dB @ 6.6 GHz −25.5 dB @ 8.5 GHz	Yes	Weak accuracy over frequency band (7.5–11.8) GHz, MAPE (23.9%), RMSE (0.673)
[26]	N/A	3 resonant frequencies 7.39, 9.43, 14.79	1.35, 2.33, 2.23	3.2, 4.9, 4.7	NA	−17 dB @ 7.39 GHz −17.6 dB @ 9.43 GHz −29.5 dB @ 14.79 GHz	Yes	Good accuracy, MAPE (11.7%), RMSE (0.109)
[28]	60 × 60	3–13	125	7.6	71, 85	−23 dB @ 1 GHz −17.2dB @ 6.7 GHz −13.9 dB @ 10.9 GHz	Yes	Weak accuracy over frequency band (8–12) GHz, MAPE (16.6%), RMSE (0.283)
[34]	N/A	5.04–5.48	8.37	5.58	80, 86	−22.6 dB @ 5.23 GHz	No	--
This work	40 × 35 × 1.57	3.1–40	171.23	9.7	88.4, 97.9	−20.7 dB @ 3.8 GHz −19.7 dB @ 6.7 GHz −34.2 dB @ 9.6 GHz	Yes	Accurate over covered BW, MAPE (4.9%), RMSE (0.041)

6. Conclusions

This paper has investigated the design and ECM extraction of a fractal slot-loaded SWB antenna, which features a measured impedance bandwidth of 171.23%, high gain, excellent radiation efficiency, and low cross-polarization, making it a good candidate for applications requiring compact and high-performance antennas in the frequency range of 3–40 GHz. We demonstrated the accuracy of our ECM in predicting our antenna's characteristics, such as the reflection coefficient and complex impedances, across the operating bandwidth. Additionally, we validated the efficacy of a dual sequential optimization approach in determining the optimal element values for the ECM.

For future work, we plan to evaluate the performance of our SWB antenna in targeted real-world applications. We also plan to use machine learning to model complex relationships between physical antenna parameters with the aim of making our ECM both accurate and computationally efficient.

Author Contributions: Conceptualization, W.A. and B.-C.S.; methodology, W.A. and B.-C.S.; software, W.A.; validation, B.-C.S., L.W. and P.P.; formal analysis, W.A.; investigation, W.A.; resources, W.A. and B.-C.S.; data curation, W.A.; writing—original draft preparation, W.A.; writing—review and editing, W.A., B.-C.S., L.W. and P.P.; visualization, W.A., B.-C.S., L.W. and P.P.; supervision, B.-C.S., L.W. and P.P.; project administration, B.-C.S. All authors have read and agreed to the published version of the manuscript.

Funding: This research received no external funding.

Data Availability Statement: The data that support the findings of this study are available from the authors upon reasonable request.

Conflicts of Interest: Author Lulu Wang was employed by the company Mayo Clinic. Author Prabakar Parthiban was employed by the company Sofant Technologies. The remaining authors declare that the research was conducted in the absence of any commercial or financial relationships that could be construed as a potential conflict of interest.

References

1. ITU. *Radio Regulations: Articles*; Int. Telecommun. Union Radiocommunication (ITU-R): Geneva, Switzerland, 2020; Volume 1.
2. Azim, R.; Islam, M.T.; Arshad, H.; Alam, M.M.; Sobahi, N.; Khan, A.I. CPW-fed super-wideband antenna with modified vertical bow-tie-shaped patch for wireless sensor networks. *IEEE Access* **2020**, *9*, 5343–5353. [CrossRef]
3. Sagne, D.; Pandhare, R.A. Design and analysis of inscribed fractal super wideband antenna for microwave applications. *Prog. Electromagn. Res. C* **2022**, *121*, 49–63. [CrossRef]
4. Khan, M.A.; Rafique, U.; Savci, H.S.; Nordin, A.N.; Kiani, S.H.; Abbas, S.M. Ultra-wideband pentagonal fractal antenna with stable radiation characteristics for microwave imaging applications. *Electronics* **2022**, *11*, 2061. [CrossRef]
5. Ullah, S.; Ruan, C.; Sadiq, M.S.; Haq, T.U.; He, W. High efficient and ultra-wide band monopole antenna for microwave imaging and communication applications. *Sensors* **2020**, *20*, 115. [CrossRef]
6. Ramanujam, P.; Arumugam, C.; Venkatesan, R.; Ponnusamy, M. Design of compact patch antenna with enhanced gain and bandwidth for 5G mm-wave applications. *IET Microw. Antennas Propag.* **2020**, *14*, 1455–1461. [CrossRef]
7. Ez-zaki, F.; Belaid, K.A.; Ahmad, S.; Belahrach, H.; Ghammaz, A.; Al-Gburi, A.J.A.; Parchin, N.O. Circuit modelling of broadband antenna using vector fitting and foster form approaches for IoT applications. *Electronics* **2022**, *11*, 3724. [CrossRef]
8. Zhang, J.-E.; Zhang, Q.; Qin, W.; Yang, W.-W.; Chen, J.-X. Compact and broadband substrate integrated dielectric resonator antenna suitable for 5G millimeter-wave communications. *IEEE Open J. Antennas Propag.* **2023**, *4*, 982–989. [CrossRef]
9. Liu, X.; Wang, X.; Yang, G.-M.; Xiang, D.; Zheng, L.-R. Dual-band frequency reconfigurable metasurface antenna for millimeter wave joint communication and radar sensing systems. *Opt. Express* **2024**, *32*, 13851–13863. [CrossRef] [PubMed]
10. Dey, S.; Karmakar, N.C. Design of novel super wide band antenna close to the fundamental dimension limit theory. *Sci. Rep.* **2020**, *10*, 16306. [CrossRef]
11. Joseph, O.; Silas, A.; Donmaaye, S.E.; Nawunzuk, T.J.; Loung, V.Y.K.; Duah, N.T. Design of a compact monopole antenna for super wideband and 5G applications. In Proceedings of the 2021 IEEE 8th International Conference on Adaptive Science and Technology (ICAST), Accra, Ghana, 25–26 November 2021; pp. 1–5.
12. Rafique, U.; ud Din, S.; Khalil, H. Compact CPW-fed super wideband planar elliptical antenna. *Int. J. Microw. Wirel. Technol.* **2021**, *13*, 407–414. [CrossRef]
13. Garg, R.K.; Singhal, S.; Tomar, R. A CPW fed clown-shaped super wideband antenna. *Prog. Electromagn. Res. Lett.* **2021**, *99*, 159–168. [CrossRef]
14. Das, S.; Mitra, D.; Chaudhuri, S.R.B. Staircase fractal loaded microstrip patch antenna for super wide band operation. *Prog. Electromagn. Res. C* **2019**, *95*, 183–194. [CrossRef]
15. de Oliveira, A.M.; Justo, J.F.; Perotoni, M.B.; Kofuji, S.T.; Neto, A.G.; Bueno, R.C.; Baudrand, H. A high directive Koch fractal Vivaldi antenna design for medical near-field microwave imaging applications. *Microw. Opt. Technol. Lett.* **2017**, *59*, 337–346. [CrossRef]
16. Kundu, S.; Chatterjee, A. A compact super wideband antenna with stable and improved radiation using super wideband frequency selective surface. *AEU-Int. J. Electron. Commun.* **2022**, *150*, 154200. [CrossRef]
17. Alamro, W.; Abdelazeez, M.K. Analysis and optimisation of super-wideband monopole antenna with tri-band notch using a transmission line model. *IET Microw. Antennas Propag.* **2019**, *13*, 1373–1381. [CrossRef]
18. Faouri, Y.; Ahmad, S.; Naseer, S.; Alhammami, K.; Awad, N.; Ghaffar, A.; Hussein, M.I. Compact super wideband frequency diversity hexagonal shaped monopole antenna with switchable rejection band. *IEEE Access* **2022**, *10*, 42321–42333. [CrossRef]
19. Agarwal, S.; Sharma, A.; Zuazola, I.J.G.; Whittow, W.G. Three-dimensional miniaturized super wideband antenna with filtering capabilities. *Int. J. RF Microw. Comput. Aided Eng.* **2022**, *32*, e23200. [CrossRef]
20. Biswas, B.; Karmakar, A. Electrical equivalent circuit modelling of various fractal inspired UWB antennas. *Frequenz* **2021**, *75*, 109–116. [CrossRef]
21. Sharma, N.; Bhatia, S.S.; Banga, V.K. Design and investigation of pocket shaped fractal antenna using circular ring elements for UWB technology with stub loaded DGS. *Int. J. Electron.* **2023**, *110*, 1516–1533. [CrossRef]
22. Mandal, S.; Karmakar, A.; Singh, H.; Mandal, S.K.; Mahapatra, R.; Mal, A.K. A miniaturized CPW-fed on-chip UWB monopole antenna with band-notch characteristics. *Int. J. Microw. Wirel. Technol.* **2020**, *12*, 95–102. [CrossRef]
23. Karmakar, A.; Biswas, B. Electrical equivalent circuit modeling of various electrically small antennas for biomedical applications. *Ann. Appl. Sci.* **2022**, *1*, 1–13. [CrossRef]
24. Sheng, X.; Zhao, X.; Liu, N.; Gao, X. Design of miniaturized FSS using equivalent circuit model and multi-objective particle swarm optimization. *J. Phys. D Appl. Phys.* **2021**, *54*, 405001. [CrossRef]

25. Khorramizadeh, M.; Nezhad, S.M.-A. Radar cross-section reduction of an UWB MIMO antenna using image theory and its equivalent circuit model. *Int. J. RF Microw. Comput. Aided Eng.* **2021**, *31*, e22563. [CrossRef]
26. Mukherjee, S.; Biswas, A. Computer aided equivalent circuit model of SIW cavity backed triple band slot antenna. *Int. J. RF Microw. Comput.-Aided Eng.* **2017**, *27*, e21060. [CrossRef]
27. Luo, S.; Chen, Y.; Wang, D.; Liao, Y.; Li, Y. A monopole UWB antenna with sextuple band-notched based on SRRs and U-shaped parasitic strips. *Int. J. Electron. Commun.* **2020**, *120*, 153206. [CrossRef]
28. Prabhu, P.; Subramani, M.; Kwak, K.S. Analysis of integrated UWB MIMO and CR antenna system using transmission line model with functional verification. *Sci. Rep.* **2022**, *12*, 14128. [CrossRef] [PubMed]
29. Al-Amin, M.R.; Li, C.; Sharawi, M.S. Full lumped element-based equivalent circuit model for connected slot antenna arrays. *IEEE Open J. Antennas Propag.* **2022**, *3*, 1273–1288. [CrossRef]
30. Esmati, Z.; Powell, D.A.; Skipper, M.C.; Abdalla, M.D.; Tyo, J.S. Development of an equivalent circuit model for the design of array of electrically small antennas. *IEEE Trans. Antennas Propag.* **2023**, *71*, 381–392. [CrossRef]
31. Balanis, C.A. Microstrip and mobile communications antennas. In *Antenna Theory: Analysis and Design*, 4th ed.; John Wiley: Hoboken, NJ, USA, 2016; pp. 815–823.
32. Ripin, N.; Sulaiman, A.A.; Rashid, N.E.A. An equivalent circuit model of miniature double E-shaped meander line printed monopole antenna. *J. Telecommun. Electron. Comput. Eng.* **2018**, *10*, 59–63.
33. Ghosal, S.; Chaudhuri, S.R.B. Analysis of a rectangular slot on a microstrip patch antenna with an equivalent circuit model. In Proceedings of the Applied Electromagnetics Conference (AEMC), Bhubaneswar, India, 18–20 December 2013.
34. Jin, C.; Shen, Z.X.; Li, R.; Alphones, A. Compact circularly polarized antenna based on quarter-mode substrate integrated waveguide sub-array. *IEEE Trans. Antennas Propag.* **2014**, *62*, 963–967. [CrossRef]
35. Deng, H.; Zhu, L.; Ouyang, J.; Peng, C.; Han, D. Single circular polarisation antenna array using a novel low profile high gain reflectarray antenna for 5G mm-wave applications. *IEEE Open J. Antennas Propag.* **2021**, *2*, 937–946.
36. Khaleel, H.R. An UWB antenna array for flexible IoT wireless systems. *Prog. Electromagn. Res.* **2018**, *162*, 109–121.
37. Shekhawat, S.S.; Lodhi, D.; Singhal, S. Dual band notched superwideband MIMO antenna for 5G and 6G applications. *AEU-Int. J. Electron. Commun.* **2024**, *184*, 155419. [CrossRef]
38. Ahmed, B.T.; Carreras, D.C.; Marin, E.G. Design and Implementation of Super Wide Band Triple Band-Notched MIMO Antennas. *Wirel. Pers Commun.* **2021**, *121*, 2757–2778. [CrossRef]
39. Dey, S.; Arefin, M.S.; Karmakar, N.C. Design and experimental analysis of a novel compact and flexible super wideband antenna for 5G. *IEEE Access* **2021**, *9*, 46698–46708. [CrossRef]
40. Ayyappan, M.; Patel, P. On design of a triple elliptical super wideband antenna for 5G applications. *IEEE Access* **2022**, *10*, 76031–76043. [CrossRef]